Transport Phenomena in Electric Smelting of Nickel Matte: Part II. Mathematical Modeling

Y.Y. SHENG, G.A. IRONS, and D.G. TISDALE

A three-dimensional mathematical model was developed to simulate the distributions of electrical potential, heat release, temperature, and velocity in the slag and matte in a six-in-line 36 MVA capacity furnace for smelting nickel calcine. From Part I of this series, it was found that there was a substantial electrical potential drop at the electrode surface, likely due to arcing through evolved carbon monoxide. The incorporation of this phenomenon into the model permitted accurate calculation of the current, power, and temperature distributions in the slag and matte. The slag was found to be thermally homogenized due to the evolved gas, and to a lesser extent by natural convection. In contrast, the matte was thermally stratified; this finding was attributed to poor momentum transfer across the slag/matte interface. Ninety percent of the electrical energy was used in smelting reactions in the calcine; to simulate the heat transfer from the slag to the calcine, a heat transfer coefficient was deduced from plant data. The implications of these findings for stable furnace operation are discussed.

I. INTRODUCTION

IN the electric smelting of nickel matte, Soderberg self-baking electrodes are used to transfer heat to the slag for calcine smelting. The electrodes are immersed in an electrically conducting slag, and it is commonly believed that the electrical energy is converted into heat by ohmic losses in the slag. Therefore, the distribution of the generated heat is principally determined by the electrical field intensity distribution and the electrical conductivity of the slag; the latter quantity is a function of the slag composition and temperature. As discussed in Part I of this article,[1] the furnace geometrical factor may be used to relate the conductivity of the slag to the resistance between electrodes. While that approach is simple, it does not yield the heat generation distribution in the slag. To obtain this distribution, Maxwell's equations[2,3] for the electric field intensity must be solved, along with the appropriate fluid flow and heat transfer equations. This is the subject of the present part of the article.

Dilawari and Szekely[4,5] were the first to tackle this class of problem; they studied electroslag remelting of steel ingots that had the similar feature of joule heating of the slag, coupled with convection in the slag. In a subsequent article, Choudhary and Szekely[6] addressed electric smelting. More recently, Jiao and Themelis[7] and Jardy *et al.*[8] used similar techniques to simulate electric furnace behavior in nonferrous smelting. However, none of these computational models has been validated with full-scale plant data. In the present article, a comprehensive mathematical model is presented to simulate the slag and matte phases in an electric furnace operated by Falconbridge Limited. The model uses plant data for some of the boundary conditions, and relies on the information acquired in the experimental investigation of the electric furnace in Part I. The computed results for electrical variables, such as electrical potential, current, and power, as well as temperature distributions in both slag and matte phases, are compared with the plant data. Computed flow fields in both the slag and the matte phases are also presented.

Y.Y. SHENG, formerly Post Doctoral Fellow with the Department of Materials Science and Engineering, McMaster University, is Research Scientist, Noranda Technology Centre, Pointe Clairs, PQ, Canada H9R 1G5. G.A. IRONS, DOFASCO/NSERC Professor of Process Metallurgy, is with the Department of Materials Science and Engineering, McMaster University, Hamilton, ON, Canada L8S 4L7. D.G. TISDALE, Process Engineer, is with the Smelter Complex, Falconbridge Limited, Falconbridge, ON, Canada P0M 1S0.

Manuscript submitted April 12, 1996.

II. MATHEMATICAL MODEL

A. *General Considerations*

In principle, this problem involves the three-dimensional, unsteady-state coupled solution of Maxwell's equations, the Navier–Stokes equation, and the associated equation for heat transfer. Three major simplifications were made to Maxwell's equations.

(1) Only steady-state solutions were sought; therefore, the alternating current was replaced by an equivalent direct current, as in the work by Szekely and co-workers.[4,5,6] In this case, a time-averaged electrical field was obtained.
(2) The magnetic Reynolds number for this system was in the range of 10^{-4} to 10^{-6}, so that the charge carried by fluid convection could be neglected because it was much less than the current due to potential gradients.[4,5,6] This eliminated one source of coupling between the electromagnetic and fluid flow equations.
(3) The other source of coupling was the electromagnetic force, or the Lorentz force, ($\mathbf{J} \times \mathbf{B}$). It was demonstrated by Choudhary and Szekely[6] for large-scale smelting furnaces that this force is negligible in comparison to natural convection forces. A similar conclusion was reached by Jardy *et al.*[8] Dimensional arguments are presented in the Appendix that show that the electromagnetic stirring force is of the order of 1 pct of the natural convection and bubble-driven forces.

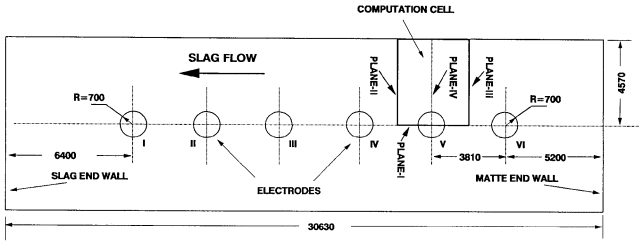

Fig. 1—Top view of the Falconbridge electric furnace for nickel smelting. Dimensions are in millimeters.

With these assumptions, Maxwell's equations[2,3] degenerated to the Laplace equation:

$$\nabla \cdot \mathbf{J} = \nabla \cdot (\sigma_s \nabla V) = 0 \qquad [1]$$

and the fluid flow equations were decoupled from Maxwell's equations.

For the steady-state solution of the momentum and heat transfer equations, the following assumptions were made.

(1) The flow was mainly laminar, but where it was turbulent, the conventional k-ε model[9] was used.
(2) As discussed in Part I, carbon monoxide bubbles were generated around the electrode due to the reduction of oxides in the slag by carbon in the electrode. The fluid flow was driven by a combination of the buoyancy of the bubbles and natural convection of the slag. As noted previously, the electromagnetic force was small and neglected.
(3) The interface between the molten slag and the matte was considered to be motionless; this assumption will be addressed in Section V.
(4) The slag was covered by a thick layer of calcine. The interface between the slag and the calcine was assumed to be an inlet for freshly smelted slag and matte to enter the slag. The falling velocities of the newly formed slag and matte were calculated from the smelting rate. Heat transfer into the calcine layer was handled with a heat transfer coefficient at the interface, based on the plant data.

B. *Mathematical Formulation*

The transport equations for steady-state momentum and heat transfer were solved in three dimensions. The three-dimensional conservation equation for a transportable variable, ϕ, is expressed in the following form:

$$\frac{\partial(\rho U\phi)}{\partial x} + \frac{\partial(\rho V\phi)}{\partial y} + \frac{\partial(\rho W\phi)}{\partial z} + \frac{\partial(J_{\phi,yz})}{\partial x} + \frac{\partial(J_{\phi,xz})}{\partial y} + \frac{\partial(J_{\phi,xy})}{\partial z} = S_\phi \qquad [2]$$

where ϕ stands for U, V, W, T, k, and ε.

The source term for the vertical momentum equation is composed of two terms: the first is the buoyancy due to the natural convection of the slag, and the second is the buoyancy of the carbon monoxide bubbles:

$$S_{W,z} = g\rho\beta\,(T - T_{\text{ref}}) + \rho_m\,\alpha g \qquad [3]$$

The second term requires some explanation. Quasi-single-phase or mixture models are most commonly used to calculate the void fraction, α, in gas-stirred systems.[10] These models require *a priori* specification of the void fraction, either from measurement or other models. The mixture density, ρ_m, is given by

$$\rho_m = (1 - \alpha)\rho_s + \alpha\rho_g \qquad [4]$$

From the measured electrode consumption rate (35 kg/h), the volumetric carbon monoxide flow rate was calculated to be 1.67×10^{-2} m^3/s at each electrode. The void fraction was estimated to be 0.03 in the first two layers of nodes around the electrode (a combined thickness of 0.24 m) and 0.01 in the next layer of nodes (0.26 m). These dimensions roughly correspond to the agitated region that was observed visually around the electrodes. The selection of the void fraction was constrained by the following arguments. The velocity of the rising gas, W_g, is related to the void fraction and the volumetric gas flow rate, Q_g, by continuity considerations:

$$W_g = \frac{Q_g}{\alpha A} \qquad [5]$$

where A is the cross-sectional area through which the gas is rising. If the selected void fraction is too large, then the gas rising velocity becomes very small; on the other hand, the source term in Eq. [3] increases with void fraction, resulting in liquid velocities that are much larger than the gas velocity, which is physically unrealistic. Conversely, if the selected void fraction is too small, then the gas velocity is much greater than the calculated liquid velocity, which would correspond to very large bubbles, which again is unreasonable. Based on these estimated void fractions, average gas bubble rising velocity is calculated to be 0.31 m/s from Eq. [5]. The computed mixture velocity is at most 0.25 m/s, so that the slip velocity is at least 0.06 m/s, corresponding to bubbles of approximately 1-mm diameter rising in the slag. In Section V, the sensitivity of the computed velocities to these assumptions is assessed. For simplicity, it was also assumed that the electrodes were cylinders, but in reality, the ends become rounded due to preferential erosion of the bottom edge. Furthermore, the gas evolution from the bottom surface was ignored, and all the gas was assumed to rise from the sides.

The electrical potential distribution in the slag was obtained by solving Eq. [2] for the diffusive components of the electrical current density. The electrical field intensity was then calculated from this distribution:

$$E = -\nabla V \qquad [6]$$

as was the electrical flux:

$$J = \sigma_s \nabla V \qquad [7]$$

The local heat release rate per unit volume of slag was calculated according to

$$p = \sigma_s E^2 \qquad [8]$$

C. *Geometry of the Computational Cell*

To reduce computer time, the computational cell was chosen as the portion of the bath heated by half of an electrode. Its location and cut-out view are shown in Figures 1 and 2, respectively. The cell is the same as, or a reflection of all other portions of the bath for all quantities, except

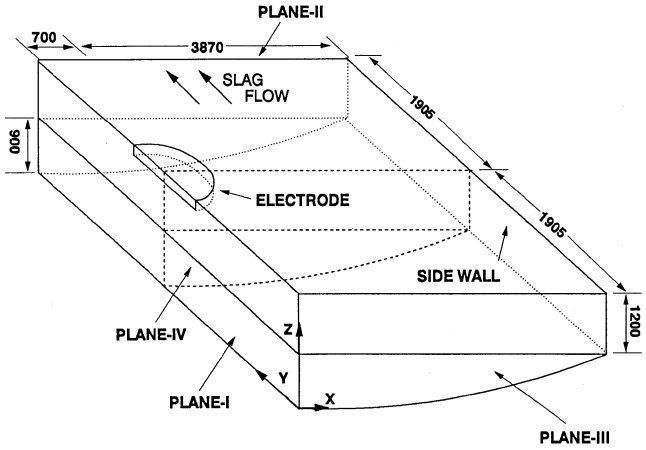

Fig. 2—A cut-out view of the computational cell. Dimensions are in millimeters.

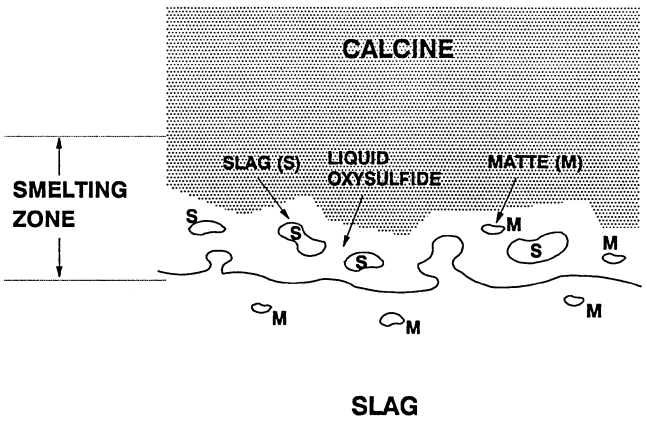

Fig. 3—Schematic view of the physical state of the smelting zone.

Table I. Relation Between Calcine Feeding Rate and Furnace Power

P (MW)	15	20	25	30	35	40
Q_c (ton/h)	35	47	58	70	80	90
q (kW/m^2)	48.2	64.3	80.4	96.4	112.5	128.6
h (kW/m^2 K)	0.32	0.43	0.54	0.64	0.75	0.86

for the net liquid flow to the tap holes. A 16 × 24 × 17 grid system was used for the computation, incorporating finer mesh near the boundaries of the fluid.

D. *Boundary Conditions*

Most of the boundary conditions took the conventional forms;[11,12] however, there were several that were distinct.

(1) Based on the smelting rate, *e.g.*, 35 tonne/h, the mass flow rates of fresh matte and slag were calculated through the calcine-slag interface. In order to maintain steady-state conditions, the same amount of slag exited in plug flow through plane II toward the slag taphole, and the same amount of matte exited through plane III toward the matte taphole. These velocities were small (each of the order of 10 μm/s) compared to the velocity caused by the rising bubbles (0.25 m/s).
(2) The heat losses to the bottom and to the calcine were derived from plant data.
(3) The slag/matte interface was assumed to be motionless.

Detailed descriptions of all the boundary conditions follow.

1. *Electrode surfaces*

The electrical potential on all surfaces of the electrode was assumed to be uniform, and equal to either the electrical potential applied to the electrode, V_e, or the electrical potential experienced by the slag, V_s:

$$V = V_e \text{ or } V = V_s \quad [9]$$

In Part I, it was shown that there was a significant electrical potential drop at the electrode surface. By changing these boundary conditions, the effects were explored. When V_s was used as the boundary condition, the heat released due to arcing at the electrode surface was treated as an extra heat source evenly distributed in the first layer of the nodes around the electrode. It was assumed that there was no heat exchange between the electrode and the slag, so that the temperature gradients perpendicular to the walls were zero. For the flow field, the non-slip-boundary condition was assumed.

2. *Slag/calcine interface*

No electrical current entered the calcine phase because it was electrically insulating. Therefore, the vertical gradient of the electric potential was zero at the interface. However, there was a surface current flow along the interface that was calculated once the electric potential field was available.

While no electric current entered the calcine, a heat balance for the entire furnace showed that 90 pct of the electrical energy supplied to the furnace was consumed in smelting reactions. Therefore, it was extremely important to properly represent the heat flow into the calcine layer where these reactions occurred. According to the investigations of Utigard *et al.*, the smelting zone is a region of semisolid oxysulfides, coke, and calcine particles from which the molten slag and matte droplets fall, as illustrated in Figure 3.[13] Because these reactions are strongly endothermic, they cannot proceed without heat from the slag. Therefore, there is a complex interplay between the rates of heat transfer, flow of reactants and products, and chemical reactions to determine the thickness and structure of the smelting zone. At our present level of understanding, it was not possible to model the smelting zone in detail, but it was necessary to provide an appropriate boundary condition, so that the governing equations for the slag and matte could be solved.

Not surprisingly, it was found that the conventional wall functions for heat transfer grossly underestimated the rate of heat transfer through the calcine-slag interface. Therefore, it was decided to model the heat transfer empirically. Table I shows the furnace power, P, required for various calcine feeding rates, Q_c. Based on the observation that 90 pct of this power was consumed in smelting and transferred though the hearth area of 280 m^2, the heat flux, q, was calculated. From observations in the plant and in the laboratory,[13] the smelting zone temperature, T_{sm}, was 1100 °C. For the conditions in Table I, the bulk slag temperature, T_{sl}, was 1250 °C. Therefore, the effective heat transfer coefficient was calculated from these two temperatures and the heat flux according to

$$q = h(T_{sl} - T_{sm}) \quad [10]$$

Table II. Physical Properties

Property	Slag	Matte
ρ (kg/m^3)[14]	3200	4500
B (K^{-1})[14]	2.7×10^{-4}	1×10^{-4}
C_p (J/kg/K)*	1250	720
μ (Pa s)	0.3[15]	0.05
ν (m^2/s)	9.38×10^{-5}	1.11×10^{-5}
k (W/m/K)[16]	8.00	17.0
α (m^2/s)	2.0×10^{-6}	5.25×10^{-6}
Pr (—)	46.9	2.11
σ_s (mho/m)	30[15]	93,000[15]

*The heat capacities were estimated from the heat capacities of the components.

For convenience, a linear regression between the furnace power and heat transfer coefficient was used in the model:

$$h = 0.321 + 21.4\ P \qquad [11]$$

where P is in MW and h is in kW/m^2/K. The physical significance of the empirical correlation will be discussed later.

As noted earlier, the calcine-slag interface was treated as a mass flow inlet to simulate the fall of fresh slag and matte into the bath. The rate was assumed to be uniform over the entire interface. A no-slip-boundary condition for the horizontal component of slag velocity was adopted.

3. *Plane I*

For this symmetry plane along the length of the furnace, it was assumed that there was no flow of momentum, heat, or electrical current across the plane. Therefore, the gradients of velocity, temperature, and electrical potential perpendicular to the plane were all set to zero.

4. *Plane II*

This plane separated the computational cell from the cell in a different electrical phase; therefore, there was no current flow across this boundary. Consequently, the electrical potential gradient perpendicular to this plane was set to zero. It was assumed that the slag flowed from the cell through this plane toward the slag tap hole. The inflow of matte from the adjacent cell was ignored for simplicity. Also for simplicity, heat losses across this boundary were not permitted, *i.e.*, the temperature gradient perpendicular to the interface was set to zero. This condition is only strictly true in the absence of mass flow across the boundary; hence, this approximation ignores the difference between the sensible heat of the inflowing and outflowing matte, which is a small quantity.

5. *Plane III*

This plane was midway between electrodes in the same phase. Using the equivalent direct current for the alternating current, this plane became a ground plane where the electrical potential was zero. In a similar manner to plane II, matte exited from this plane toward the matte taphole, and it was assumed to be a symmetry plane for heat transfer.

6. *Sidewall of the furnace*

Since there was no current flow in the refractory walls, the gradient of the electric potential perpendicular to the side walls of the furnace was zero. The furnace was operated with copper coolers in the side walls so that a thin solid slag layer protected the refractory. Therefore, the side wall temperature was fixed at the melting point of the slag, 1050 °C. The conventional no-slip-boundary condition was used for momentum transfer.

7. *Bottom of the furnace*

Similar to plane III, this boundary was also assumed to be a ground plane with zero electric potential. For the temperature field, typical heat fluxes extracted by fans beneath the furnace shell were used. For momentum transfer, the bottom wall was treated as a nonslip wall.

8. *Matte/slag interface*

The interface was considered motionless, as mentioned earlier. Consequently, both sides of the interface were treated as nonslip walls. With this boundary condition, heat was only transferred by conduction. Continuity of the heat flux across the interface was prescribed.

III. PHYSICAL PROPERTIES OF SLAG AND MATTE

The physical properties of the slag and matte at 1250 °C are listed in Table II. The temperature dependencies of the density, viscosity, and slag conductivity were obtained from various references.[14,15,16]

IV. COMPUTATIONAL RESULTS

The mathematical model was solved by using the commercial computational fluid dynamics code, PHOENICS.[17] Three cases with different boundary conditions at the electrode surface were examined with the model:

(1) no potential difference at the electrode surface (the electrical potential applied to the electrode, V_e (160 V), equalled the electrical potential experienced by the slag, V_s);
(2) same as case 1, but the electrical potential experienced by the slag was 100 V; and
(3) a 160 V electrical potential applied to the electrode with a 60 V drop at the electrode surface so that the slag experienced 100 V (the heat due to the 60 V drop was released adjacent to the electrode).

A. *Electrical Potential and Power Distributions*

The electrical potential distributions in planes I and IV for the first two cases are shown in Figures 4 and 5, respectively. (The electrical potential distribution in the slag for case 3 is virtually the same as for case 2.) The corresponding volumetric heat release distributions for the three cases are shown in Figures 6 and 7. It is clear that the heat release rate drops even more sharply away from the electrode than does the electrical potential. This finding can be understood by examination of Eqs. [5] and [7], which show that the heat release rate depends on the square of the potential gradient. The highest heat release rates at the electrode surface were obtained in case 3 as a result of the extra potential drop at the electrode surface (Figures 6(c) and 7(c)). The calculated phase current and the total power released in the furnace for the three cases are shown in Figure 8, along with the range of plant data for these two variables. Only with the inclusion of the electrode surface potential

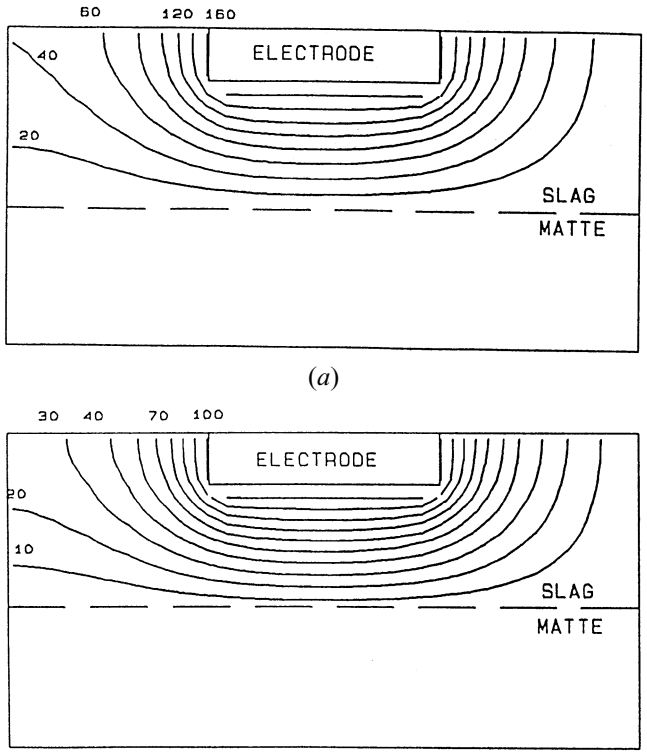

Fig. 4—Calculated distributions of the electrical potential (volts) in plane I for (*a*) case 1 and (*b*) case 2.

drop and extra heat source for the heat released in the vicinity of the electrode do both the calculated current and furnace power fall in the range of the operational data. In Part I, it was also shown that the potential drop at the electrode surface was essential to match the operational voltage distributions.

B. *Flow Fields*

The calculated flow fields for the three cases are all very similar, so only the flow field for case 2 is shown in Figure 9. The flow is generated by natural convection and bubble stirring; consequently, the flow is strongest around the electrode, where maximum velocities are approximately 0.25 m/s. Away from the electrode, the bulk slag velocity is of the order of 0.02 m/s. There are two areas of recirculation in the slag.

(1) A plume near the electrode entrains slag from below the electrode and then radiates across the slag/calcine interface. This is the principle recirculatory flow in the bath.
(2) There is a weaker recirculatory loop downward at the side wall area due to natural convection at the cooled wall.

If the gas evolution is turned off in the code, then the flow is driven only by the natural convection. The velocities around the electrode are approximately 0.03 m/s, several times slower than with gas evolution. Therefore, the flow is driven mainly by the buoyancy of carbon monoxide bubbles formed at the electrode surface.

As a result of the assumption of a motionless interface between the matte and the slag phase, the momentum of the slag phase is not transferred to the lower matte phase. The matte velocity is negligible, except near the curved side wall, where natural convection creates a weak recirculatory zone.

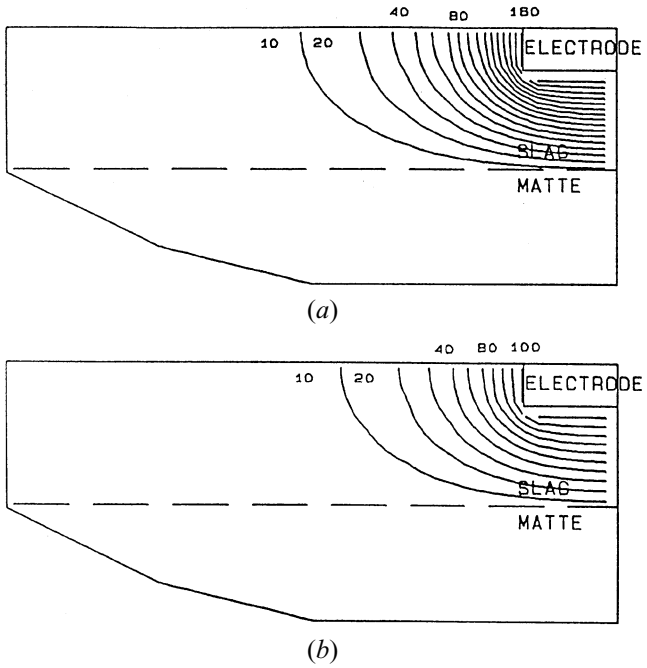

Fig. 5—Calculated distributions of the electrical potential (volts) in plane IV for (*a*) case 1 and (*b*) case 2.

C. *Temperature Distributions*

The calculated bath temperature distributions in planes I and IV are shown in Figures 10 and 11 for cases 2 and 3. (The temperature distributions for case 1 are not shown because they are similar to case 3.) In both cases, the slag phase was thermally homogenized due to the convection from bubble stirring. In contrast, the matte phase remained stratified as a result of the relatively stagnant conditions in the matte. In all three cases, the calculated slag temperatures between the electrodes ranged from 1240 °C to 1270 °C. In actual production, the slag temperature was normally in the range of 1210 °C to 1290 °C. Very good agreement between the calculated bath temperature profile and the plant data for one operating condition is shown in Figure 12. It is clearly seen that the slag was much more homogenous than the matte.

D. *Slag Resistance*

In Part I, a constant slag conductivity was assumed. In this part, the empirical correlation proposed by Jiao and Themelis[18] for conductivity was used (Figure 2 in Part I).[1] A conductivity that increases with temperature is inherently unstable; if the temperature increases, Eq. [7] shows that more power will be drawn, leading to further increases in the temperature. This instability sometimes caused the program to diverge. The problem was solved by under-relaxation of temperature changes, and by limiting the conductivity to 60 mho/m, corresponding to the highest temperature normally encountered in production (Figure 2

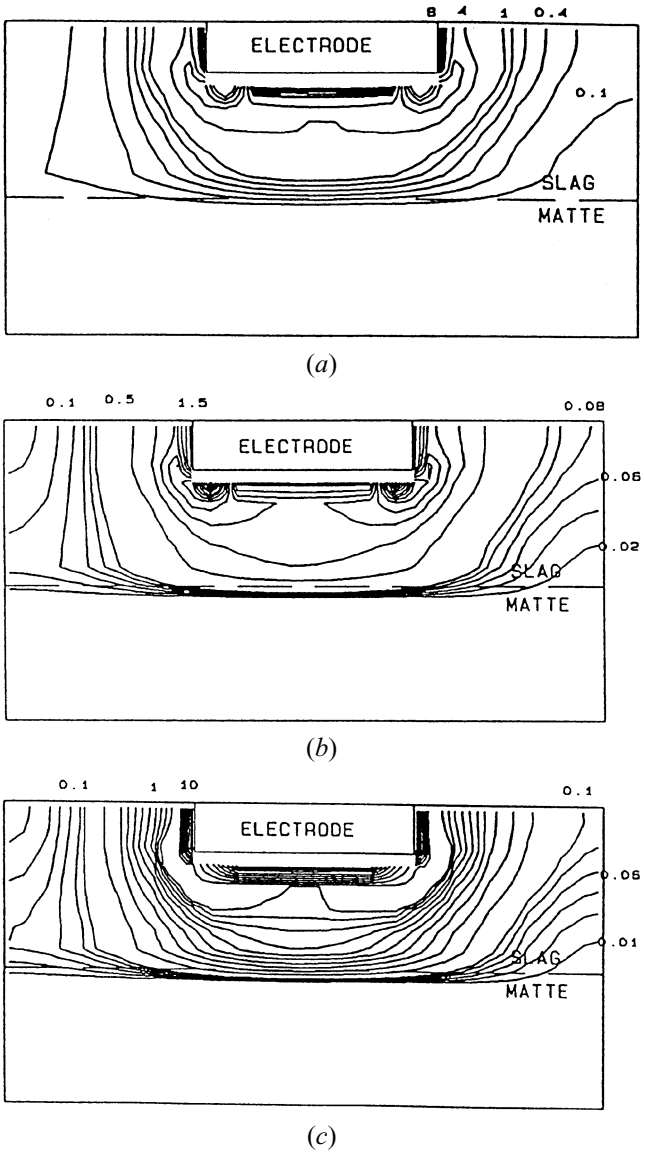

Fig. 6—Calculated distributions of the electrical power generation rate (W/m^3) in plane I for the three cases: (*a*) case 1, (*b*) case 2, and (*c*) case 3.

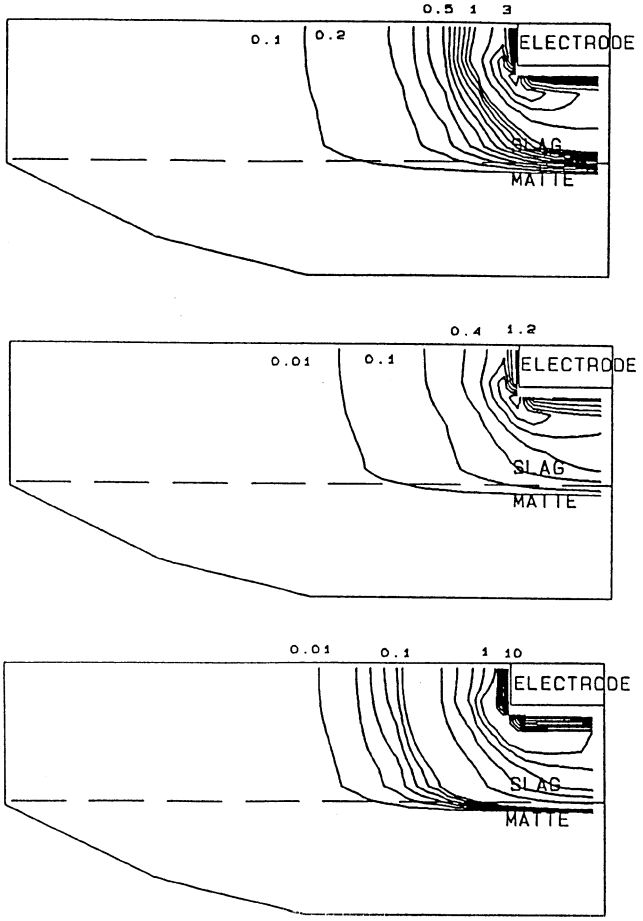

Fig. 7—Calculated distributions of the electrical power generation rate (W/m^3) in plane III for the three cases.

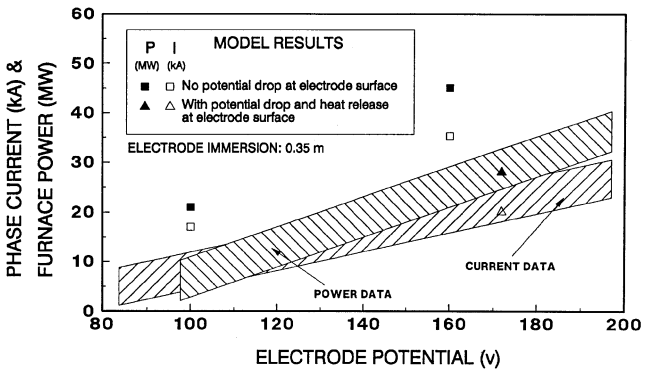

Fig. 8—Comparison between the calculated phase current and power with plant data for cases 1, 2, and 3.

in Part I). The calculations in Figures 10 and 11 show that slag temperatures are relatively uniform, providing justification for the constant conductivity assumed in Part I.

V. DISCUSSION

A. *Electrical Potential Drop at the Electrode Surface*

The results of Part I and the present mathematical model clearly indicate the existence of the electrical potential drop at the electrode surface. This finding is very important to both furnace control and furnace modeling. Without taking this phenomenon into consideration, the calculated power and electrical current in slag would have been much higher than the plant data (Figure 8). The cause of the electrical potential drop at the electrode surface is most likely arcing through carbon monoxide generated at the electrode. The relations between the electrical potential drop at the electrode surface and other electrical parameters were estimated from the model results and plant data.[19] Since the heating rate is proportional to the square of the electrical potential gradient, much more heat is generated in the immediate vicinity of the electrode (Figure 6(c)) than one would expect without consideration of the arcing (Figures 6(a) and (b)). Further investigation in this direction is required to fully explore the phenomenon for the benefit of furnace control.

While there is no doubt that gas is evolved at the electrode surface, the exact behavior of the gas is unknown. In

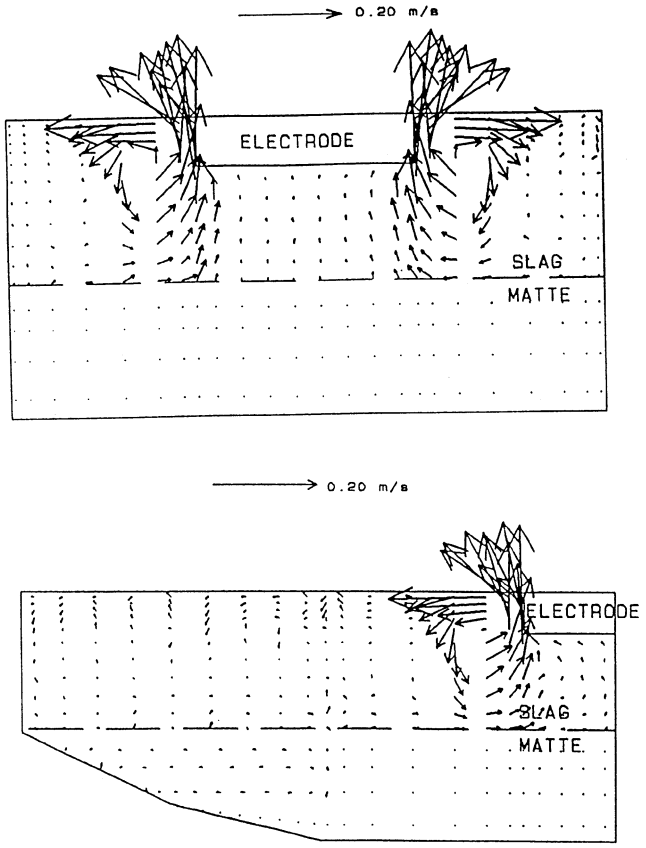

Fig. 9—Computed flow field for case 2 in planes I and IV.

Section II–B, it was argued that the void fraction must be of the order of 0.01 to 0.03, and based on this assumption, the momentum source terms were calculated. If the void fraction were doubled in the nodes around the electrodes, then the maximum computed mixture velocity rose from 0.25 to 0.38 m/s, a 52 pct increase. (These doubled void fraction values moved the flow into an unrealistic regime; the gas rising velocity from Eq. [5] dropped to 0.15 m/s, which was less than the mixture velocity.) By doubling the void fractions, the velocities away from the electrode were not changed very much, nor were the temperature distributions because the slag was already homogenized in the original calculation. Therefore, the computed results are not overly sensitive to changes in the void fraction, recognizing that the range of realistic void fraction values is restricted by the considerations in Section II–B. Consequently, the present model captures the essential aspects of the electric potential drop and the bubble-driven flow at the electrode surface; neither of these aspects has been considered in previous work on electric furnace modeling.[6,7,8] However, more detailed aspects regarding interactions between the arc and the fluids are unclear, such as the precise distribution of the gas and the current path. Most multiphase models require *a priori* knowledge of the flow regime to calculate void fraction, velocity, and temperature; the electrical phenomena further complicate this task. Experimental determination of these quantities in the near-electrode region is hampered by the high temperatures, high power levels, and corrosive nature of the slag. These formidable fundamental and practical barriers limit a more detailed understanding at this time.

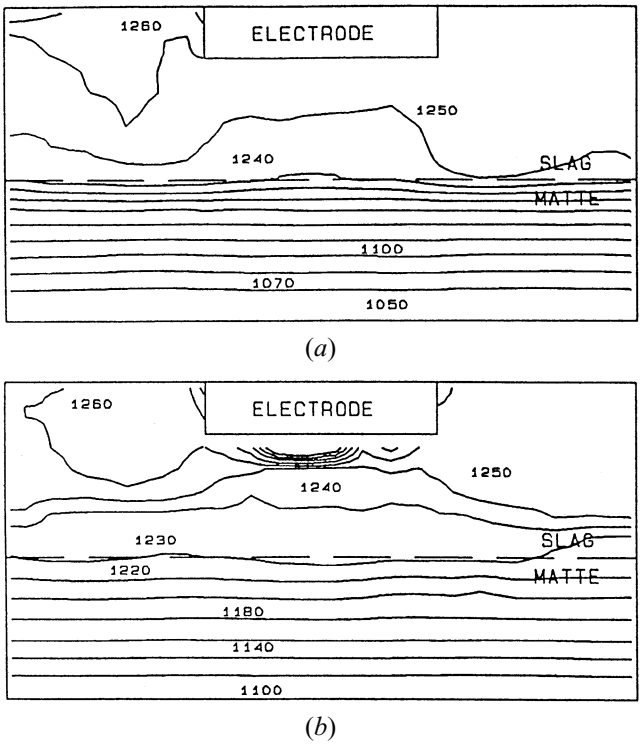

Fig. 10—Calculated distributions of the bath temperature (°C) in plane I: (*a*) case 2 and (*b*) case 3.

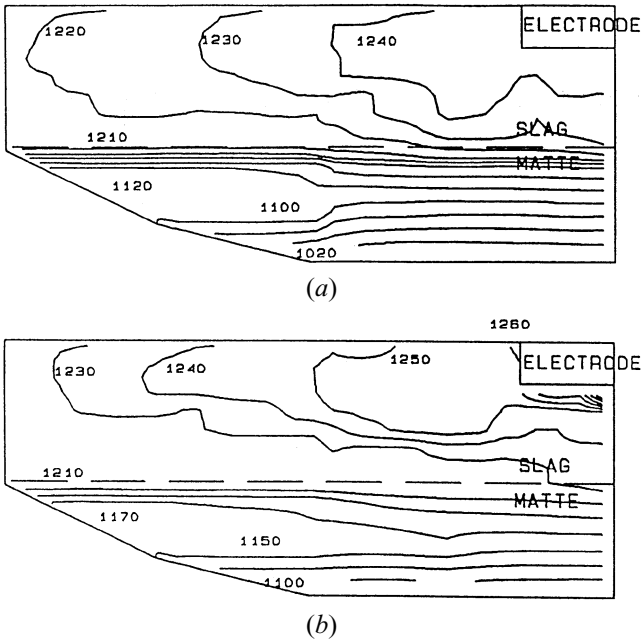

Fig. 11—Calculated distributions of the bath temperature (°C) in plane IV: (*a*) case 2 and (*b*) case 3.

B. *Slag/Calcine interface*

Plant data indicate that in this particular furnace the calcine feeding rate is proportional to the power input, and that about 90 pct of the total power input to the slag is

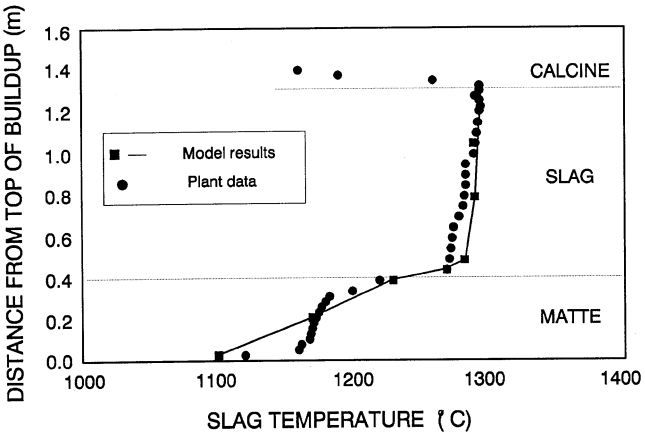

Fig. 12—Comparison between the calculated bath temperature profile and plant data.

transferred to the smelting zone across the interface. As argued in Section II–D the conventional wall function approach is inappropriate for the slag/calcine interface because of the endothermic heat demand and the mushy nature of the interface. To ensure that the proper amount of heat was transferred to the calcine, empirical heat transfer coefficients were employed. A heat transfer coefficient is a reasonable approach, because convection is sufficient to maintain a relatively homogenous slag temperature despite the very high heat flux. It is interesting to note that if the gas stirring is turned off in the code, then there is significant overheating of the slag around the electrode. Thus, the gas evolution at the electrode is a fortuitous aspect, which apparently ensures that convection in the slag phase is fast enough not to control the smelting rate. While the empirical correlation works well in the power range covered by the available plant data, it must be noted that there may be a point at which the smelting rate is not proportional to the power input. In such conditions, a more detailed understanding of the smelting mechanism would be required.

C. *Matte/Slag Interface*

It was found that a no-slip boundary condition at the matte/slag interface was required to achieve good agreement between the measured and computed temperature profiles. If the boundary conditions are changed to permit horizontal velocities in the matte and slag at the interface, then the matte becomes thermally homogenized, which is at odds with experimental measurement. There are two hypotheses to explain the immobile behavior of the interface.

The first hypothesis may be found in the literature related to immobilization of interfaces.[20,21] In that work, force balances are made between surface shear forces and those due to surface tension gradients. These concepts have been successfully applied to immobilization of bubble interfaces,[22] but there has been much less work on large planar interfaces pertinent to the present work. Mansell and co-workers[23,24] investigated the interface between a fluid flowing in a channel and another immiscible fluid inside a square cavity below the channel. They used the following equation as a boundary condition:

$$\tau_{xy}^{-} - \tau_{xy}^{+} = \frac{d\sigma_o}{dy} \qquad [12]$$

where τ_{xy}^{+} is the shear from the upper, moving layer; τ_{xy}^{-} is resisting shear in the lower liquid; and σ_0 is the surface tension. This equation may be used to provide an explanation for the immobile behavior of the interface. At the side wall of the vessel, the interface is restrained, so that the horizontal and vertical velocities are zero. At the centerline, a similar boundary condition exists due to symmetry, although in reality, the point of flow separation may oscillate. The interface may be postulated to move only when the shear stress above the interface overcomes the interfacial tension holding the interface rigid; *i.e.*, the shear stress times the interfacial area must exceed resisting force due to interfacial tension. From the mathematical model, the average shear stress in the upper liquid at the interface is 0.005 to 0.01 Pa. The resulting total shear force along the interface of length 5 m and unit width is approximately 0.03 to 0.05 N. The interfacial tension between matte and slag is 300 to 500 mN/m.[25] The restraining force due to interfacial tension over unit width is therefore 0.3 to 0.5 N; consequently, the interface remains motionless. According to these calculations, the shear stress could be increased tenfold before the interface would stretch.

The other hypothesis is that the interface is immobilized by the presence of a solid phase at the interface. Scrap materials are charged to the furnace for their nickel and cobalt values, but the materials also contain chromium. The quantity of chromium-containing material is strictly limited because the chromium is oxidized, and its oxide has only limited solubility in the slag. In poorly controlled conditions, the solid chromia may accumulate at the bottom of the furnace or create a ''false bottom'' at the interface between the slag and matte. While such conditions were not observed in the present work, it is inevitable that there was some chromia in the system, which must settle to or through the slag/matte interface. Given the weak shear stresses discussed in the previous paragraph, a thin layer of chromia may impede the motion of the interface.

D. *Implications for Furnace Operation*

As discussed in Section IV–D, the fact that slag conductivity increases with temperature creates an inherently unstable situation. As well as making the mathematical model unstable, it likely destabilizes actual furnace operation. If the temperature increases due to some process disturbance, then the conductivity also increases, which in turn draws more power into the furnace, further increasing the temperature. The operator must then try to correct by reducing current or voltage or by increasing resistance by reducing electrode immersion. The effect of reduced electrode immersion on the ohmic resistance of the slag, *i.e.*, ignoring the potential drop at the electrode surface, is shown in Figure 13. The difficulty in reducing the electrode immersion is that the current is carried through a smaller portion of the electrode tip, accelerating the erosion in this region. It may also be seen from Figure 13 that smaller electrodes have even higher resistance, which means that this corrective action is also intrinsically unstable. Higher resistance and the correspondingly higher current density and temperatures are responsible for rounding of the electrodes.

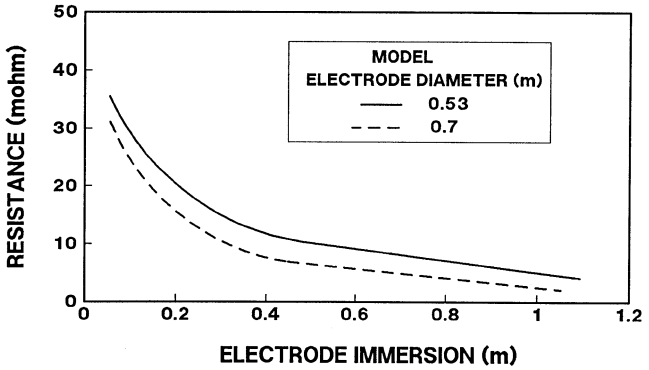

Fig. 13—Calculated ohmic resistance of the slag alone between two electrodes as a function of the electrode immersion.

The thermal stratification in the matte seen in Figures 10 and 11 is quite striking. It is a result of two phenomena:

(1) heating the furnace from the top and cooling it from the bottom; and
(2) the poor transfer of momentum through the slag/matte interface.

This sometimes leads to operational problems such as the precipitation of iron-nickel metallics, which settle to the bottom of the furnace. It is difficult to overcome such problems. In a previous study using a low-temperature, nonisothermal physical model of this furnace, it was shown that gas injection could homogenize the temperature distribution in the furnace.[26] However, the homogenization only occurred in the melt above the end of the lance tip. To homogenize the matte, lances would be required to withstand immersion through both the slag and matte.

These two examples indicate the importance of transport phenomena on the practical operation of an electric smelting furnace. They also highlight a need for continued work to improve the fundamental understanding of furnace operation.

VI. CONCLUSIONS

This is the first three-dimensional mathematical model of an electric furnace for nickel smelting that has been tested against full-scale plant data. The findings of the present investigation are summarized as follows.

1. The mathematical results are consistent with a sharp drop of the electrical potential at the electrode surface. Such a drop is likely caused by the arcing between the slag and the electrode through carbon monoxide evolved at the electrode surface.
2. Electrical power is released in the bath in two steps: first, by arcing at the electrode surface; and second, by Joule heating in the bulk of the slag. In some instances, the portion of the power released in the vicinity of the electrode in the form of arcing was more than half of the total power input.
3. To correctly calculate slag temperature, the heat flux across the calcine-slag interface, which comprises about 90 pct of the total heat input, must be properly represented. Conventional treatment based on the assumption of a solid wall for the calculation of the heat flux significantly underestimates the heat flux. An empirical correlation produced better agreement, but its validity beyond the present power input levels is uncertain.
4. The motion of the slag is driven mainly by the gas bubbles evolved at the electrode interface, and to a lesser extent by natural convection. Bubble-driven flow had not been considered in previous work. Consistent with previous work, the electromagnetic stirring force is much smaller than the natural convection forces.
5. Because the slag conductivity increases with temperature, an inherently unstable situation is created. This phenomenon affects the stability of the mathematical model and is likely a feature of actual furnace operation.
6. In this furnace, the slag is reasonably homogenous in temperature, whereas the matte is stratified. The gas evolution at the electrodes stirs the slag, but momentum transfer to the matte is poor. Because the furnace is heated from the top and cooled from the bottom, the matte is stably stratified.
7. The electrical resistance of the slag increases as the electrode immersion is decreased. From a control standpoint, this is also inherently unstable and leads to rounding of the ends of the electrodes.

APPENDIX

The relative magnitudes of the stirring forces can be estimated by calculating the characteristic velocities for the slag that would be generated by each stirring mechanism. Choudhary and Szekely[6] made order-of-magnitude estimates, based on dimensional arguments. For electromagnetic stirring, the characteristic velocity is of the order of

$$U_o \approx \sqrt{\frac{\mu_m}{\rho_s}}\, J_o\, L_o \qquad [A1]$$

where J_0 and L_0 are the characteristic electrical current density and length scale, respectively. For natural convection, the velocity is

$$U_o \approx \sqrt{\beta g L_o \Delta T_o} \qquad [A2]$$

where ΔT_0 is the characteristic temperature difference driving the flow. By similar considerations, the velocity created by gas-stirred convection is

$$U_o \approx \sqrt{\frac{\rho_m}{\rho_s}\, \alpha_o g L_o} \qquad [A3]$$

where α_0 is the characteristic void fraction. For the present configuration, the electrode diameter was selected as the characteristic length scale. The characteristic current density at the electrode surface, based on 10 kA, was 2670 A/m^2. The characteristic temperature difference was taken as 50 K. The characteristic void fraction was estimated to be 0.02, based on the discussions in Section II–B. Inserting these values into the three previous equations, the characteristic velocities for electromagnetic stirring, natural convection-driven flow, and bubble-induced stirring are 0.074, 0.43, and 0.52 m/s, respectively. The electromagnetic velocity is only 8 pct of the other two. However, it is more appropriate to consider the relative magnitudes of forces, which are proportional to the square of these velocities. Therefore, for the present configuration, the electro-

magnetic stirring force is only 1 pct of the other two forces combined.

ACKNOWLEDGMENTS

The authors are very grateful to Falconbridge, Limited, for supporting this project and permitting publication of this article. The encouraging comments from Falconbridge personnel, including Mr. I.A. Cameron and Dr. G. O'Connell, are greatly appreciated. Useful discussions with Professor T. Utigard and his colleagues at the University of Toronto, as well as the assistance of Mr. O. Kelly and Falconbridge's smelter technicians and furnace operators, are also gratefully acknowledged. The assistance of CHAM with the use of PHOENICS is also acknowledged.

NOMENCLATURE

C_p	heat capacity (J/kg/K)
D_e	electrode diameter (m)
E	electric field intensity (V/m)
g	gravitational acceleration (m/s^2)
h	heat transfer coefficient (W/m^2/K)
H_e	immersion of the electrode in slag (m)
I	electrical current (A)
J	conduction current density (A/m^2) or flux in Eq. [2]
k	thermal conductivity (W/m/K)
L	length scale (m)
P	electrical power input of the furnace (MW)
p	power generation rate per unit volume (W/m^3)
Pr	Prandtl Number, ν/α (—)
q_{sw}	heat flux at the side wall (W/m^2)
Q_c	calcine feeding rate (tonne/h)
R_s	electrical resistance of slag (ohm)
Re_m	magnetic Reynolds number, LU/α_m (—)
S	source term in conservation equations
t	time (s)
T	temperature (K)
V	electrical potential (V)
V_e	electrical potential applied to the electrode (V)
V_s	electrical potential experienced by the slag (V)
U, V, W	velocities (m/s)
x, y, z	coordinates (m)
α	thermal diffusivity (m^2/s) or gas void fraction (—)
α_m	magnetic diffusivity, $1/\sigma_e\mu_m$ (m^2/s)
β	coefficient of thermal expansion (K^{-1})
μ	viscosity (Pa s)
μ_m	magnetic permeability (Henry/m)
v	kinematic viscosity (m^2/s)
ρ_m	density of the slag-gas mixture (kg/m^3)
ρ_s	density of the slag (kg/m^3)
ρ_g	density of the gas (kg/m^3)
σ_0	surface tension (J/m)
σ_s	electrical conductivity of slag (mho/m)
τ	shear stress (J/m^2)
ϕ	transportable variable

REFERENCES

1. Y.Y. Sheng, G.A. Irons, and D.G. Tisdale: *Metall. Mater. Trans. B*, 1998, vol. 29B, pp. 77-83.
2. J.D. Kraus and K.R. Carver: *Electromagnetics*, 2nd ed., McGraw-Hill Book Company, New York, NY, 1973.
3. W.F. Hughes and F.J. Young: *The Electromagnetodynamics of Fluid*, Wiley, New York, NY, 1966.
4. A.H. Dilawari and J. Szekely: *Metall. Trans. B*, 1977, vol. 8B, pp. 227-36.
5. A.H. Dilawari and J. Szekely: *Metall. Trans. B*, 1978, vol. 9B, pp. 77-87.
6. M. Choudhary and J. Szekely: *Mineral Process Extractive Metall., Trans. IMMO*, 1981, Sect. C, vol. 90, pp. 164-73.
7. Q. Jiao and N.J. Themelis: Paper presented at *Conf. of Metallurgists*, Winnipeg, MB, Aug. 23–26, 1987, CIM, Montreal, 1987.
8. A. Jardy, D. Ablitzer, and S. Jorget: *Proc. Reinhardt Schuhmann Int. Symp. on Innovative Technology and Reactor Design in Extractive Metallurgy*, D.R. Gaskell, J.P. Hager, J.E. Hoffmann, and P.J. Mackey, eds., Colorado Springs, CO, Nov. 9–12, 1986, TMS-AIME, Warrendale, PA, 1986.
9. W. Rodi: ''*Turbulence Models and Their Application in Hydraulics*,'' 2nd ed., State-of-the-Art Paper, Presented by the IAHR–Section on Fundamentals of Division II: Experimental and Mathematical Fluid Dynamics, Delft, The Netherlands, 1984.
10. D. Mazumdar and R.I.L. Guthrie: *Iron Steel Inst. Jpn. Int.*, 1995, vol. 35, pp. 1-20.
11. T. Deb Roy, A.K. Majumdar and D.B. Spalding: *Appl. Math. Modeling*, 1978, vol. 2, pp. 146-50.
12. D. Mazumdar and R.I.L. Guthrie: *Metall. Trans. B*, 1985, vol. 16B, pp. 83-90.
13. T.A. Utigard, A. Warczok, and M. Zamalloa: ''Increased Calcine Smelting Rate,'' Final Report, Falconbridge Limited, Falconbridge, ON, Apr. 1994.
14. J.N. Hryn: Master's Thesis, University of Toronto, Toronto, 1982.
15. N.M. Stubina, G.H. Kaiura, H. Tseng, and J.M. Toguri: ''To Develop a Clean Smelting Process for Highly Roasted Copper-Nickel Calcines and to Improve Metal Recovery, Part D: Electrical Conductivity Measurements of Electric Furnace Smelting Slags,'' DSS File No. 15SQ.23440-3-9172, University of Toronto, Toronto, 1988.
16. Falconbridge Limited, Falconbridge, ON, unpublished research, 1995.
17. CHAM: *PHOENICS™ Manuals*, Version 1.6.6, London, 1992.
18. Q. Jiao and N.J. Themelis: *Metall. Trans. B*, 1991, vol. 22B, pp. 183-92.
19. Y.Y. Sheng, G.A. Irons, and D.G. Tisdale: *Proc. Quality in Non-Ferrous Pyrometallurgy*, 34th Annual COM, Vancouver, BC, Canada, Aug. 20–23, 1995, M.A. Kozlowski, R. W. McBean, and S.A. Argyropoulos, eds., TMS-CIM, Toronto, 1995, pp. 265-78.
20. L.E. Scriven: *Chem. Eng. Sci.*, 1960, vol. 12, pp. 98-108.
21. C.V. Sternling and L.E. Scriven: *AlChE J.*, 1959, vol. 5 (4) pp. 514-23.
22. R. Clift, J.R. Grace, and M.E. Weber: *Bubbles, Drops and Particles*, Academic Press Inc., New York, NY, 1978, pp. 36-41.
23. G.E. Mansell, R.S. Hickman, and E. Marschall: *Proc. 3rd ASME/JSME Thermal Engineering Joint Conf.*, Part 2 (of 5), ASME, New York, NY, 1991, pp. 109-17.
24. G.E. Mansell, J. Walter, and E. Marschall: *J. Computat. Phys.*, 1994, vol. 110, pp. 274-84.
25. S.W. Ip and J.M. Toguri: *Metall. Trans. B*, 1993, vol. 24B, pp. 657-68.
26. S.K. Banerjee and G.A. Irons: *Can. Metall. Q.*, 1992, vol. 31 (1), pp. 31-40.